applied mechanics

MDPI

Article

Fault Detection in Offshore Structures: Influence of Sensor Number, Placement and Quality

Andreas Tockner *, Jixiang Lei and Katrin Ellermann

Institute of Mechanics, Graz University of Technology, Kopernikusgasse 24/IV, 8010 Graz, Austria; jixiang.lei@tugraz.at (J.L.) ellermann@tugraz.at (K.E.)
* Correspondence: andreas.tockner@tugraz.at

Abstract: Within the Space@Sea project floating offshore islands, designed as an assembly of platforms, are used to create space in offshore environments. Offshore structures are exposed to harsh environment conditions. High wind speeds, heavy rainfall, ice and wave forces lead to highly stressed structures. The platforms at the Space@Sea project are connected by ropes and fenders. There exists the risk of a rope failing which is therefore investigated subsequently. To ensure the safety of the structure, the rope parameters are monitored by the Extended Kalman Filter (EKF). For platform arrangements, a large number of sensors is required for accurate fault diagnosis of these ropes, leading to high investment costs. This paper presents a strategy to optimize the number and placement of acceleration sensors attached to the floating platforms. There are also high demands on the sensors due to the harsh offshore conditions. Material deterioration and overloading may lead to decayed sensor performance or sensor defects. Maintenance of offshore sensors is difficult, expensive and often not feasible within a short time. Therefore, sensor measurement deviations must not affect reliable structure fault detection. The influence of defect sensors on the rope fault detection is examined in this study: Types, intensities, number, place of occurrence of defect sensors and the distance between defect sensors and rope faults are varied.

Keywords: sensor fault; sensor placement; extended Kalman filter; offshore structure; multi body dynamics; floating islands

Citation: Tockner, A.; Lei, J.; Ellermann, K. Fault Detection in Offshore Structures: Influence of Sensor Number, Placement and Quality. *Appl. Mech.* **2022**, *3*, 757–778. https://doi.org/10.3390/applmech3030045

Received: 14 April 2022
Accepted: 21 June 2022
Published: 27 June 2022

1. Introduction

Sensors are used in almost every complex technical application and are indispensable in daily life. Applications of sensors range from environmental monitoring, disease detection, machinery and vehicle monitoring to robots and agriculture [1]. They also play a major role in maritime applications such as logistic and shipping activities, to stay on course and to prevent collisions, for characterizing the hydrodynamic performance of designed hulls and machinery performance monitoring to detect failures, to optimize the fuel consumption and to reduce environmental pollution [2]. For characterizing hydrodynamic performance in the work of [3] among others acceleration sensors are used to investigate the heave and pitch motions of a ship on the resistance and the ice-breaking pattern. In [4] floating-plate-type friction sensors are used to measure the friction reduction in an experimental setting using air lubrication of the bottom of a flat plate. Examples for machinery performance monitoring are given in [5] where the diagnosis of the coking of a marine diesel engine injector nozzle is performed by measuring and analysing the vibrations of the crankshaft and the study [6] use level sensors to estimate the position and size of a breach of a damaged ship. Offshore sensors are established for arctic field observation, e.g., to observe the arctic warming, CO_2 and methane fluxes due to climate change [7,8].

Another sensor application is safety monitoring of offshore structures. Structure fatigue, corrosion, abrasion and external unwanted effects decrease structural safety. An

outline of field monitoring of offshore structures and related sensor technologies is given in [9]. The work of [10] uses sensor data and cosine similarity for multi damage detection. Ref. [11] uses fibre bragg grating sensors and [12] ambient excitation for structure health monitoring of offshore structures. Corrosion monitoring of a ship structure is shown in [13] where mainly optical, acoustic, electromagnetic and galvanic sensors are used. Examples of offshore riser monitoring can be found in [14] where fibre optic strain sensors monitor the static and dynamic strain of offshore risers and in [15] acceleration measurement data are used for monitoring riser damage due to wave and vortex-induced-vibration. Fault detection in mooring lines of a floating offshore wind turbine is given in [16], further work for mooring monitoring is done by [17].

This study is based on the impact of acceleration sensor data variation used for the Kalman filtering (KF) technique to estimate parameters in offshore structures from which faults in the structure are concluded. Sensor data variation is caused by different number and placement of sensors and potential sensor defects. The KF plays a major role in technical applications, some of them are given in [18,19]. The KF is an optimal filter to obtain least square estimates by combining the information of the measured information with the state prediction [20]. The input and measured values of a system are used for the KF to estimate the states and parameter of a system whereas the quality and the amount of measurement data influence the performance of the KF significantly. There are some studies on Kalman filter applications in the offshore sector. In the work of [16] the KF is used for the detection of mooring line faults in floating offshore wind turbines. In [21], hydrodynamic coefficients matrices for an offshore tower are determined by the Extended Kalman Filter (EKF).

Depending on the KF application, different sensors are used. For KF application in chemistry, the measurements of, e.g., current, potential and concentrations serve as input values [22], for moving object tracking by the KF, position and velocity are the measurement inputs measured by GPS, radar, sonar, laser and speedometers [23], for multi-body dynamics (MBD) state estimation by KF mainly inertia sensors for acceleration, vibration, inclination, displacement and gyroscopic sensors are used. Parameter estimation in MBD's with many degrees of freedom by the KF algorithm often requires many sensors to get adequate input data for the filter algorithm. More sensors provide more data, which leads basically to more precise estimation results by the KF technique, with the drawbacks of expensive hardware components and higher computational effort. Optimal sensor placement minimizes the number of sensors used for KF applications. An overview of methods for optimal decisions on the number, placement and type of sensors and actuators is given in [24].

Offshore structures are exposed to harsh environment loads, high wind speed, icy conditions and heavy wave forces overloading the structure and its superstructures. Permanent monitoring of the dynamic behaviour can be required to ensure the safety of these structures. In the European Union Space@Sea project a concept to create space in marine environment using flexible floating platforms is designed [25], areas of application of floating offshore platform arrangements are given in more detail in [26,27]. This arrangement consists of platform elements and some mooring elements attached to the corner platforms, an example of such a platform arrangement is shown in Figure 1.

Depending on the number of connected platforms, this leads to a dynamic system with many degrees of freedom. The platform elements and connecting elements of these platforms are highly stressed due to tremendous forces caused by the harsh offshore conditions. The connecting elements consist of ropes and fenders. The ropes are assumed to be the critical elements, because there are only three ropes but twelve fenders per platform side [28]. Because of the difficult accessibility to the ropes, local inspection is not feasible. Therefore, the KF technique is used to estimate the rope stiffness parameters. Based on these parameters, rope faults are detected without direct access to the damaged components. Acceleration sensors are attached to the floating platforms, delivering measurement data for the KF algorithm. Large platform arrangements lead to significant costs for sensor and

measurement data equipment with adequate quality to get sufficient results by the KF algorithm. The increasing computational effort of the KF algorithm using many sensors must be considered to maintain real-time capability. Therefore, it is of great interest to minimize the number of sensors while ensuring sufficient reliability in detecting rope faults.

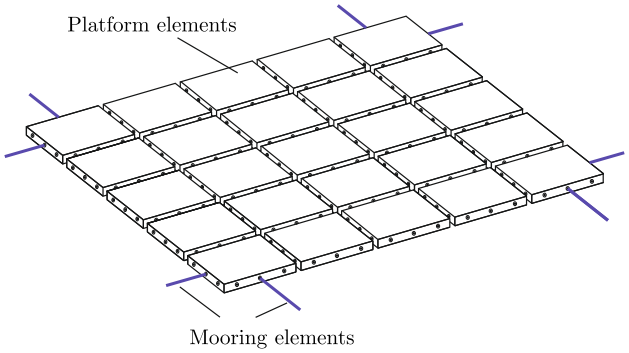

Figure 1. Example of a floating platform arrangement with mooring lines on the corner platforms.

Defect sensors or sensor failure lead to wrong measurement data, which can lead to dangerous or even disastrous consequences for people and equipment. The influence of defect acceleration sensors on the estimation of seismic fragility of structures, controlled by a linear quadratic Gaussian control and a KF algorithm, where the accuracy of the working sensors is degraded by an uniform random noise signal, is shown in [29]. For offshore applications sensor maintenance is more expensive and time-consuming. Defect sensors with scaled measurement amplitude occurring in wind turbines, often located offshore, and their detection is shown in [30]. To ensure adequate access for maintenance of the sensors and the data transfer equipment, they are exposed to potentially challenging environmental conditions, increasing the risk of damage or failure of a sensor. Defective sensors are leading to a partial or complete loss of their functionality, caused by external impacts such as temperature and corrosion or by internal influences as component wear and overheating. An overview of common types of defect sensors and possible reasons for their occurrence is given in [1]. A study of defect sensors occurring in sensor networks and their modelling is shown in [31]. According to [31], defect sensors can be described by environment, system and data characteristics. For offshore applications, environment features such as physical conditions such as environmental perturbations caused by weather conditions such as heavy rain, hail, icing, strong sunlight and ambient conditions such as salinity and humidity can lead to defective sensors. Errors in the measurement system can be caused by a defective transducer, a defective analog to digital converter, exceeding the detection range, component degradation due to the age of the sensors, a weak power supply, e.g., low batteries for wireless sensors and noise caused by unwanted variation in the data. Wrong sensor calibration leads to faulty measurement values.

The first aim of this work is to minimize the number of acceleration sensors used for rope fault detection by the EKF while ensuring sufficient fault detection reliability. Therefore, a strategy for optimal sensor placement is developed. The challenge of this optimal sensor placement strategy is that it must be suitable for complex nonlinear systems with a large number of degrees of freedom and sensors. Another aim is to determine the influence of the numbers, location of occurrence and intensity of different types of sensor defects on the reliability of rope fault detection. The advantages and disadvantages of using an additional sensor per platform are presented in detail. The investigations concerning sensor placement, sensor defects and fault detection in the connecting elements are based on a platform arrangement consisting of 25 platforms with 150 degrees of freedom. The original software used for the presented methodology was developed in-house.

This paper is structured as follows: First, the MBD model of the platform arrangement is designed and a short introduction to the KF theory is given in Section 2. In Section 3, a strategy of optimal sensor placement for rope fault estimation is developed and applied

to a platform arrangement. Starting from the two most efficient sensor placements, the influence of different sensor defects on the rope fault detection reliability is investigated in Section 4. Section 5 discusses the results of different quantities, locations of occurrence and intensities of the defect sensors on the reliability of rope fault detection. Finally, a conclusion is given in Section 6.

2. Problem Description

The system described subsequently is based on an example of a platform configuration of the Space@Sea project. The platform arrangement does not exist at the time of this work. In this section, a MBD model of the platform arrangement is built up to simulate the model of the platform arrangement which creates necessary measurement data for the KF algorithm. The KF, a short description of its algorithm is given subsequently, estimates the rope stiffness of the MBD platform model. Based on deviations of the estimated rope stiffness from the stiffness of non-faulty ropes, rope faults are concluded.

2.1. System Kinematics

A 5 × 5 platform array with 25 platforms, 30 connecting ropes, 3 acceleration sensors per platform and 8 mooring lines, attached to the corner platforms, is shown in Figure 2a. The mooring lines are attached to the corner platforms to keep the platform arrangement in place. They are designed as non-prestressed linear springs in horizontal direction which cannot transmit compression forces. Fibre ropes and elastomer fenders connect the floating platforms. Their modelling is shown for platforms 21–25 in Figure 2c. The prestressed fibre ropes are attached to the exterior platforms. They go through pipes inside the platform elements and are connected to the edge or corner platforms on the opposite side of the platform array as shown in Figures 2c and 3.

The platforms are made of concrete, the fenders consist of rubber with steel flanges which are used to connect the platform elements. Forces and moments acting on a single platform are shown in Figure 2b. The equations of motion of a single platform are given according to [28]. They are given by

$$\ddot{x} = \frac{1}{m_{pf} + mx_{add}} \left[\sum_{j=0}^{a\,n_r} Fc_{rx(j)} + Fc_{mx} + \sum_{j=0}^{a\,n_f} \left(Fc_{fx(j)} + Fd_{fx(j)} \right) + Fdv_x + Fd_x \right], \quad (1)$$

$$\ddot{y} = \frac{1}{m_{pf} + my_{add}} \left[\sum_{j=0}^{a\,n_r} Fc_{ry(j)} + Fc_{my} + \sum_{j=0}^{a\,n_f} \left(Fc_{fy(j)} + Fd_{fy(j)} \right) + Fdv_y + Fd_y \right], \quad (2)$$

$$\ddot{z} = \frac{1}{m_{pf} + mz_{add}} \left[\sum_{j=0}^{a\,n_r} Fc_{rz(j)} + \sum_{j=0}^{a\,n_f} \left(Fc_{fz(j)} + Fd_{fz(j)} \right) + Fb_z + F_g + Fd_z \right], \quad (3)$$

$$\ddot{\varphi}_x = \frac{1}{\Theta_{pf_x} + \Theta x_{xadd}} \left[\sum_{j=0}^{a\,n_r} Mc_{rx(j)} + \sum_{j=0}^{a\,n_f} \left(Mc_{fx(j)} + Md_{fx(j)} \right) + Md_x + Mb_x \right], \quad (4)$$

$$\ddot{\varphi}_y = \frac{1}{\Theta_{pf_y} + \Theta y_{yadd}} \left[\sum_{j=0}^{a\,n_r} Mc_{ry(j)} + \sum_{j=0}^{a\,n_f} \left(Mc_{fy(j)} + Md_{fy(j)} \right) + Md_y + Mb_y \right], \quad (5)$$

$$\ddot{\varphi}_x = \frac{1}{\Theta_{pf_z}} \left[\sum_{j=0}^{a\,n_r} Mc_{rz(j)} + \sum_{j=0}^{a\,n_f} \left(Mc_{fz(j)} + Md_{fz(j)} \right) \right], \quad (6)$$

where Fc_r are the forces and Mc_r the moments acting from the fibre ropes on the platform. The forces Fc_f and Fd_f and the moments Mc_f and Md_f are generated from the fender stiffness and fender damping. The indices x, y and z refer to the directions of the forces and to the axes of rotation of the moments. The mooring line forces Fc_m act on the platforms on the corners of the platform arrangement and are considered only for them. The damping of the platform caused by the interaction of the ocean current and the platform motion is accounted for by Fd and Md, the linear damping forces and linear damping moments, and Fdv, the viscose damping forces. The buoyancy is respected by the buoyancy force Fb respectively the buoyancy moments Mb, the weight by F_g. The buoyancy force is calculated from the amount of water displaced by the platform, calculated from the difference of

the platform location and the average wave height projected to the platform area, the buoyancy moment by the inclined position of the platform around the φ_x and the φ_y axis. The platform mass is named m_{pf} and the platform inertia related to their x, y and z axes Θ_{pf_x}, Θ_{pf_y} and Θ_{pf_z}. The impact of the surrounding fluid is respected by the additional mass mx_{add}, my_{add} and mz_{add}, the additional inertia terms Θx_{add}, Θy_{add} and Θz_{add} and also by the linear damping forces Fd_x, Fd_y and Fd_z and linear damping moments Md_x and Md_y. The factor a represents the number of adjacent platforms which is four for a platform inside the platform array, three for a platform in the corner and two for a platform at the edge of the platform array. The number of ropes and the number of fenders per platform side area are given by n_r and n_f. The wave height is calculated from the Pierson- Moskowitz power spectrum [32] using autoregressive moving averages [33].

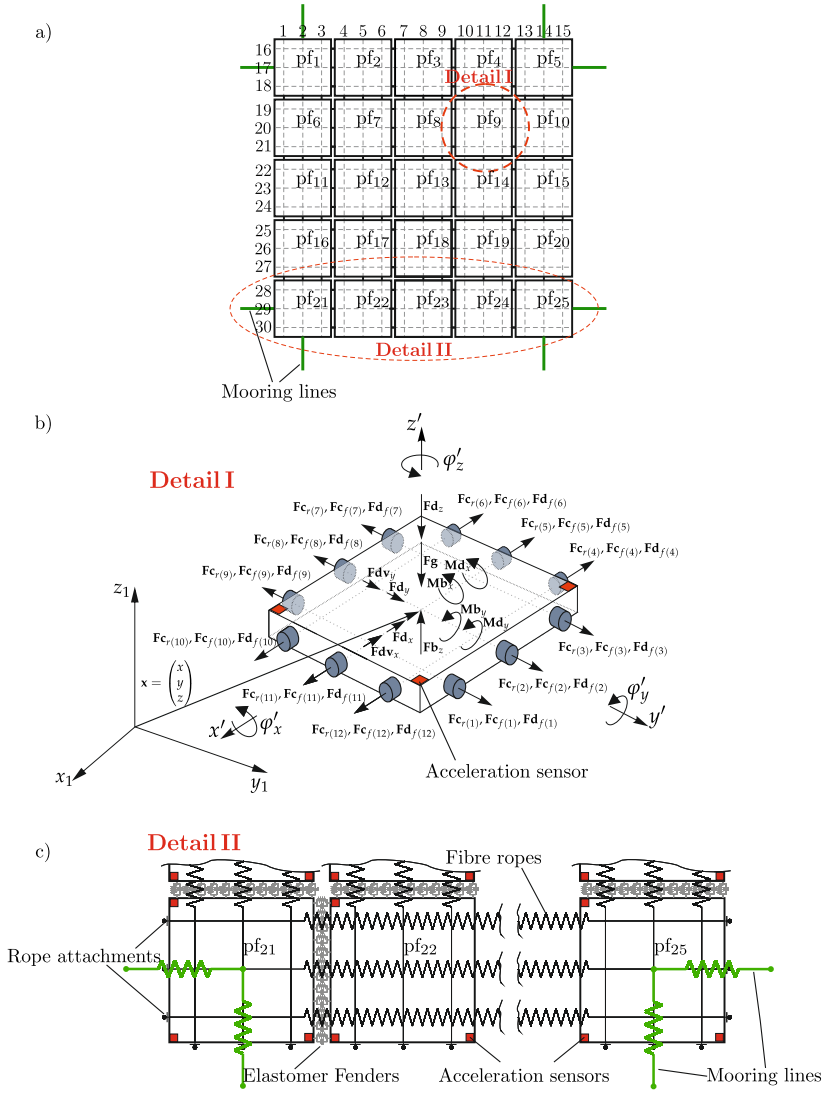

Figure 2. (**a**) Platform arrangement of 25 platforms and 30 ropes. (**b**) Forces and moments acting on a single platform. (**c**) Detailed schematic representation of several platform connections (**c**).

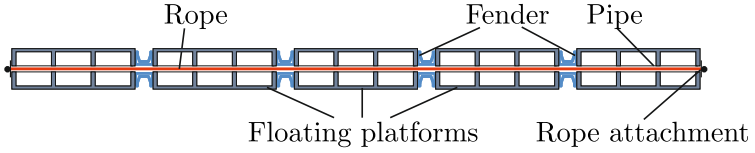

Figure 3. Schematic sectional view of five floating platforms connected by ropes and fenders.

2.2. Rope Fault Estimation Using EKF

The EKF is an extension of the linear KF to account for non-linearities in the system and measurement equations [20]. The system and measurement equations of a non-linear discretized system are described by

$$x_k = f_{k-1}(x_{k-1}, u_{k-1}, w_{k-1}), \tag{7}$$
$$y_k = h_k(x_k, v_k), \tag{8}$$

where x_k are the states calculated by the state function f_{k-1} including the previous states x_{k-1}, the system input u_{k-1} and the process noise w_{k-1}, the measurements y_k are calculated by the measurement function h_k including the states x_k and the measurement noise v_k. The Kalman observer should estimate the states and the parameters of the MBD model by using the model input u_k and the acceleration measurements y_k, shown in the schematic diagram in Figure 4.

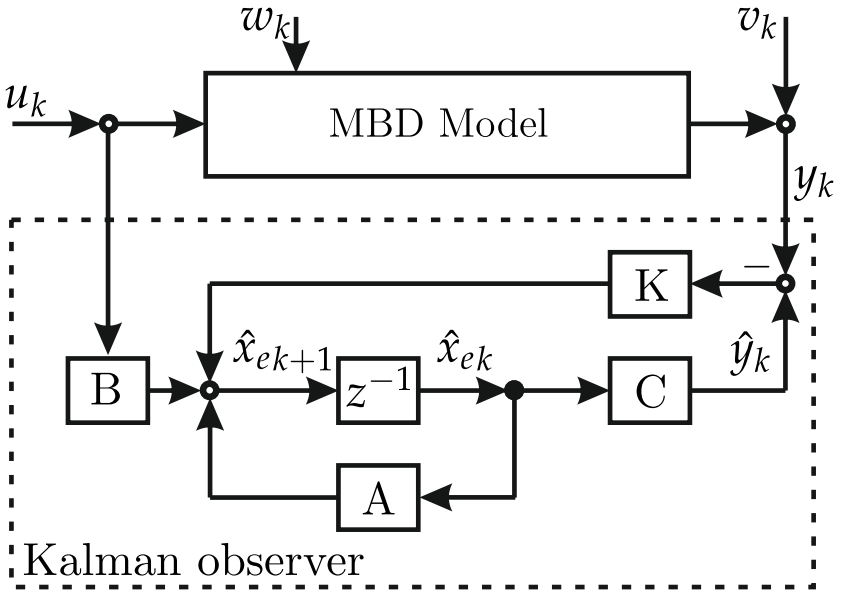

Figure 4. Schematic diagram of the dynamic system observed by the Kalman Filter (KF).

The estimated state vector $\hat{\mathbf{x}}_{\mathbf{e}_k}$ of the Kalman observer contains the estimated states of the MBD system and the states for the parameters to be estimated $\hat{\mathbf{x}}_{\mathbf{p}_k}$ resulting in $\hat{\mathbf{x}}_{\mathbf{e_k}} = [\hat{\mathbf{x}}_k^T, \hat{\mathbf{x}}_{\mathbf{p}_k}^T]^T$, $\mathbb{R}^{(n_{st}+n_p)\times 1}$. The number of states and parameters are indicated by n_{st} respectively n_p. At first the expected values of the initial state $\hat{\mathbf{x}}_{\mathbf{e}_0}^+ = E(\mathbf{x}_{\mathbf{e}_0})$ are calculated by the covariance of the initial state $\mathbf{x}_{\mathbf{e}_0}$. This results in the initial covariance of the estimated error calculated from

$$P_{e_0}^+ = E[(\mathbf{x}_{\mathbf{e}_0} - \hat{\mathbf{x}}_{\mathbf{e}_0}^+)(\mathbf{x}_{\mathbf{e}_0} - \hat{\mathbf{x}}_{\mathbf{e}_0}^+)^T]. \tag{9}$$

The estimated state $\hat{\mathbf{x}}_{\mathbf{e}_k}^-$, the time update of the covariance $P_{e_k}^-$ of the estimated error, the Kalman gain K_k, the state update $\hat{\mathbf{x}}_{\mathbf{e}_k}^+$ and the update of the covariance matrix $P_{e_k}^+$ are calculated from

$$\hat{\mathbf{x}}_{\mathbf{e}_k}^- = f_{k-1}(\mathbf{x}_{\mathbf{e}_{k-1}}^+, \mathbf{u}_{k-1}) \tag{10}$$
$$P_{e_k}^- = A_{k-1} P_{e_{k-1}}^+ A_{k-1}^T + Q_k \tag{11}$$
$$K_k = P_{e_k}^- C_k^T (C_k P_{e_k}^- C_k^T + R_k)^{-1} \tag{12}$$
$$\hat{\mathbf{x}}_{\mathbf{e}_k}^+ = \hat{\mathbf{x}}_{\mathbf{e}_k}^- + K_k \left[\mathbf{y}_k - h_k(\hat{\mathbf{x}}_{\mathbf{e}_k}^-)\right] \tag{13}$$
$$P_{e_k}^+ = (I - K_k C_k) P_{e_k}^-. \tag{14}$$

Calculation steps where the measurement information is not implied at time step k are marked by $^{(-)}$, calculation steps where the measurement information at time step k is included are marked by $^{(+)}$. The process covariance matrix Q_k is known from the process noise $\mathbf{w}_k$, $\mathbf{w}_k \sim (\mathbf{0}, Q_k)$ and the measurement covariance matrix R_k from the measurement noise $\mathbf{v}_k$, $\mathbf{v}_k \sim (\mathbf{0}, R_k)$. The nonlinearities in the system are considered by the linearized state transition matrix A_{k-1}, calculated from a partial derivative of the state function f_{k-1} near $\hat{\mathbf{x}}^{+}_{\mathbf{e}_{k-1}}$ and the linearized output matrix C_k, calculated from a partial derivative of the measurement equation h_k near $\hat{\mathbf{x}}^{-}_{\mathbf{e}_k}$ by

$$A_{k-1} = \frac{\partial f_{k-1}}{\partial \mathbf{x}_{\mathbf{e}_k}}\Big|_{\mathbf{x}_{\mathbf{e}_k}=\hat{\mathbf{x}}^{+}_{\mathbf{e}_{k-1}}} \in \mathbb{R}^{(n_{st}+n_p)\times(n_{st}+n_p)} \tag{15}$$

$$C_k = \frac{\partial h_k}{\partial \mathbf{x}_{\mathbf{e}k}}\Big|_{\mathbf{x}_{\mathbf{e}k}=\hat{\mathbf{x}}^{-}_{\mathbf{e}_k}} \in \mathbb{R}^{(n_{meas})\times(n_{st}+n_p)}. \tag{16}$$

The number of measurements is denoted by n_{meas}. To include parameter changes due to different loading or wave conditions, the platform masses, the vertical damping values and the additional masses in z direction of the MBD model are varied according to the work of [28]. The MBD model of the floating connected platforms is modified to set rope faults by lowering the stiffness of the faulty fibre ropes. The EKF should detect these faults through estimation of the respective rope stiffness. Therefore, the estimated parameters in the vector $\hat{\mathbf{x}}_{\mathbf{p}_k}$, which are part of the estimated state vector $\hat{\mathbf{x}}_{\mathbf{e}_k}$, refer to the respective corresponding rope stiffness values in the platform model. If the estimated rope stiffness parameter falls below a defined boundary, a fault in the respective rope is indicated. The state vector of the MBD model of a single platform is given by

$$\mathbf{x} = [x\ \dot{x}\ y\ \dot{y}\ z\ \dot{z}\ \varphi_x\ \dot{\varphi}_x\ \varphi_y\ \dot{\varphi}_y\ \varphi_z\ \dot{\varphi}_z]^T, \tag{17}$$

where the platform positions are given by (x, y, z) and the orientations by $(\varphi_x, \varphi_y, \varphi_z)$. For a platform arrangement consisting of 25 platforms and 30 ropes this results in 300 states (n_{st}) and 30 rope stiffness parameters (n_p) to estimate by the EKF.

The simulation of the MBD model and the EKF algorithm are calculated by the software package *MATLAB*® *R*2019a.

3. Optimal Sensor Placement for Rope Fault Detection Using EKF

States and parameters are estimated by the Kalman observer using the system input and the measurement data. The input information of the system depends on the wave spectrum and the measurement data of the acceleration sensors attached to the platforms. A previous study on fault detection in modular offshore platform connections by the EKF uses a large number of seven acceleration sensors per platform which corresponds to 175 sensors for a 5×5 platform arrangement [28]. In this section, a strategy is developed to find the optimal sensor location for a floating platform arrangement with the intention to reduce the number of sensors while ensuring reliable rope fault detection. The influence of rope faults on the measured acceleration values is investigated to find the optimal sensor locations. It is assumed that acceleration measurements of sensors which are more influenced by rope faults, deliver more valuable information to the EKF algorithm for rope fault detection. Based on these results, the influence of different sensor arrangements on the rope fault detection performance is examined to prove the previous assumption. The influence of sensor placement using ten different sensor settings, shown in Figure 5, on the percentage of correctly detected rope faults and rope fault detection time is investigated. The sensors S_1, S_3, S_7, and S_9 used for the simulations in Figure 5 are located at the corners of the platforms, the sensors S_2 and S_4 at the center of the edge, and the sensor S_5 at the center of the platform. The arrows indicates the direction of the acceleration measurements.

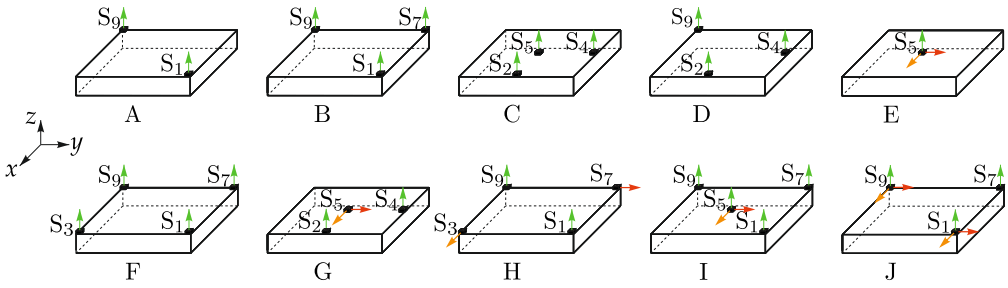

Figure 5. Sensor settings for 2, 3, 4, 6 and 7 acceleration measurements per platform.

To compare measurement data of the platform array with a fault in a rope with the measurement data from the faultless platform arrangement, measurement data of nine contemplated sensor locations and 27 acceleration measurements per platform, shown in Figure 6, are used.

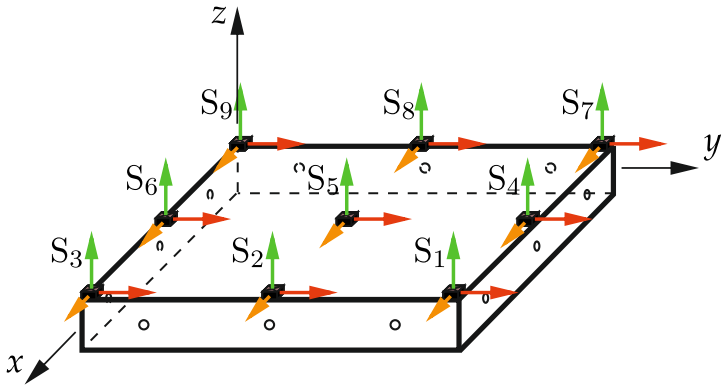

Figure 6. Contemplated locations for acceleration sensor placements measuring accelerations in x, y and z direction.

In order to be able to service the sensors, they are placed on the top of the platforms. For a 5×5 platform arrangement, shown in Figure 2a, using 30 ropes for platform connection, 30 simulations with respective one fault in a different rope are executed. To simulate the rope fault, the stiffness of the faulty rope is set to 80% of the faultless rope in the MBD model. The wind speed is set to 21 m/s measured 19.5 m above sea level and the simulation time is set to 1000 s which corresponds to 20,000 time steps. From these simulations, the average deviations of acceleration values, measured at platforms with faulty ropes y_{fault} from those at platforms without faulty ropes y_{no_fault}, are calculated by

$$y_{diff} = \frac{1}{n_{rt}} \sum_{j=1}^{n_{rt}} \sqrt{\frac{1}{n_{mtst}} \sum_{i=1}^{n_{mtst}} \left[y_{fault_{(i)}} - y_{no\_fault_{(i)}} \right]^2}, \mathbb{R}^{(n_{pf}\, n_{s_{max}}) \times 1}, \tag{18}$$

where n_{rt} is the number of simulations with respectively different rope faults, n_{mtst} the number of measurement time steps, n_{pf} the number of platforms and $n_{s_{max}}$ the number of considered acceleration measurements. An array consisting of 25 platforms, with 27 acceleration measurements each, results in 675 averaged acceleration deviation values y_{diff}. The deviating acceleration values are averaged over all platforms, where the average of the acceleration values of the sensors with the same placement and orientation of the different platforms is calculated. That gives 27 averaged acceleration deviation values y_{diffav}, corresponding to 27 signal channels shown in Figure 7. The orange bars show the averaged acceleration deviation values y_{diffav} in x direction, the red bars in y direction and the green bars in z direction. The higher these values, the greater the effect of a rope error on the acceleration measurements of the respective sensors. The indices 1 to 9 indicate the sensor number.

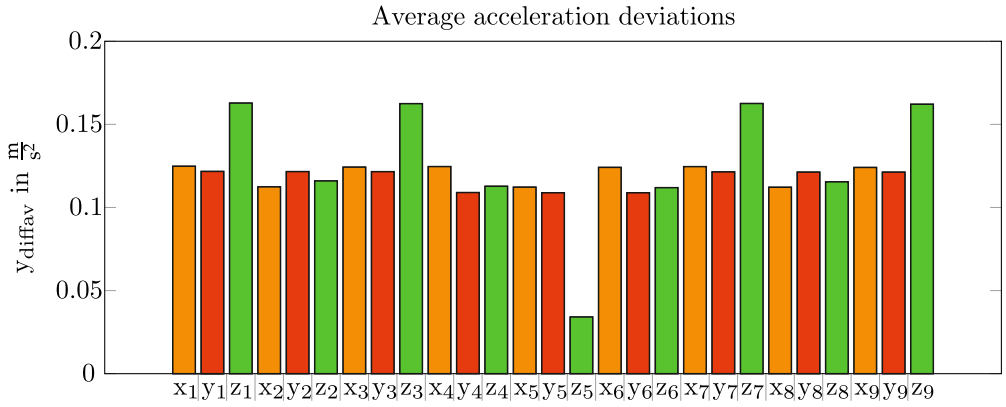

Figure 7. Over all platforms averaged acceleration deviations calculated from the difference of platform arrangements with faulty ropes and faultless ropes.

Figure 7 shows that rope faults mainly influence the acceleration values z_1, z_3, z_7 and z_9 measured by the sensors in z direction placed on the corner of the platforms and at least the z acceleration measurement z_5 in the middle of the platform. It is concluded that the z acceleration measurements of the corner sensors are more sensitive to rope faults and therefore can be considered as the main indicators for stiffness changes.

To verify this, the influence of different sensor arrangements on the rope fault detection performance is examined. Investigations are performed with 2, 3, 4, 6 and 7 acceleration measurements per platform, which are shown in Figure 5. The number and positions of the acceleration sensors on all platforms in the platform arrangement are kept the same. As rope faults detection quality in the x and y direction should be similar, symmetrical sensor arrangements are considered. Rope fault detection in rope number 8 of the 5×5 platform array is reviewed. To test the repeatability, every configuration was simulated 100 times for the same wave spectrum but a different time-depending wave height curve. The simulation starts when the MBD model is in equilibrium and not moving. The rope stiffness of the faulty rope number 8 of the MBD model the 5×5 platform model is set to 80% of the faultless value after a simulation time of 410 s, the fault detection process is launched 400 s after the simulation start. Fault detection in rope number 8 is chosen, since faults occurring in the ropes going through the centre of a platform and are placed further inside the platform arrangement are more difficult to be detected than ropes at the edges [28]. If these faults are indicated within a certain detection time, it is assumed that all other rope faults can also be reliably detected.

Table 1 lists the error detection results for the different sensor settings. The second column indicates the percentage of simulations for each sensor setting, where the faulty rope is estimated correctly within 600 s after the fault occurred. The rope fault detection times listed in the third column result from the average fault detection times of the respective 100 simulations, whereas only the fault detection times of the correctly detected faults are respected.

It can be confirmed that acceleration sensors measuring the acceleration in z direction on the corners of the platform are best suitable for EKF rope fault detection. They deliver the most important information to the EKF algorithm to estimate the movement dynamics and rope stiffness parameters of the platform arrangement. The average detection time of version B and F is the lowest compared to the other considered sensor settings. Version F leads to faster fault detection than Version B, although it can be assumed that for a rigid-body 3 sensors in z direction deliver the same information to the EKF than 4. The additional sensor in version F provides additional information to the EKF algorithm, hence measurement uncertainties due to sensor noise are compensated using 4 sensors in setting F. Fault detection for sensor setting I is faster compared to sensor setting B with the drawback of 3 additional sensors. More sensors do not always lead to better results. The comparison of sensor setting J with sensor setting B shows longer fault detection time and only 99%

of correctly detected rope faults for the sensor setting J with 4 additional acceleration sensors given in Table 1. Additional data of the acceleration sensors in x and y direction reduce the weighting of the acceleration sensors data in z direction, where the EKF gets the predominant information from.

Table 1. Fault detection parameters for 2, 3, 4, 5 and 7 acceleration measurements per platform.

Sensor Setting	Correct Fault Indication in %	Rope Fault Detection Time s
A	17	531
B	100	107
C	100	288
D	100	142
E	0	-
F	100	77
G	82	387
H	74	419
I	100	100
J	99	150

4. Influence of Sensor Defects on the Reliability of Rope Fault Detection

In this chapter, the influence of the number, placement and intensity of sensor defects on the reliability of rope fault detection at the 5×5 platform arrangement is investigated by the EKF. Defect sensors lead to sensor data deviation from the correct measured sensor data. Sensor data from defective sensors used for KF input leads to less accurate state and parameter estimation.

4.1. Sensor Defects

Material deterioration, overloading and environmental corrosion mandatory lead to degraded sensor performance or sensor defects [34]. Typical sensor defects are bias, drift, gain, precision degradation and complete failure with constant sensor output with or without sensor noise [35], detailed description and causes of some sensor defects are shown in the work of [1]. In this work, sensor defects refer to sensor precision degradation, sensor gain defects, sensor bias and complete sensor defects. Insufficient power supply or hardware failures can degrade sensor precision due to additional noise. A precision degradation can be defined as an unexpectedly high amount of variation exceeding the expected variance of the sensor given by the sensor manufacturer. The possibility of higher environmental noise must be considered and may not be related to a sensor error [1,31]. Sensor gain defects occur when the rate of change of the measured acceleration data deviates from the true sensor values. This results in a wrong scaled measurement amplitude. Reasons for sensor gain defects can be calibration faults, measuring signal amplifier faults, unstable voltage supply, or non-linearity of the sensor [31,36]. Insufficient zero-point or temperature calibration of the sensor can cause sensor bias defects. Furthermore, bias voltage or bias current, caused by an unstable change of environment temperature, lead to sensor bias defects [1].

The simulation of the MBD platform model creates measurement data used for the KF algorithm for rope fault detection. To simulate defects in specific sensors of the MBD model, the measurement values of the respective defect sensors are altered. Sensor precision degradation is simulated by gaussian white noise with a variance up to 1 m^2/s^4, which is added to the measurement values of the sensors, where a defect is introduced. For sensor gain defects, the defect sensor measurement amplitudes are calculated by $y^*(t) = \Delta\, y(t)$ where $y(t)$ are the faultless sensor measurements received from the MBD model. For the simulations, a range of Δ dependent on the sensor defect intensity from 0.5 to 1 is chosen. Sensor bias defects are simulated by adding a constant value of 0.1 up to 1.5 m/s^2 to the measurement values of the MBD model, where a sensor defect is simulated. The parameters of the different sensor defects used for the simulations are listed in Table 2.

Table 2. Parameters of the simulated sensor defects.

Kind of Sensor Defect	Parameter	Parameter Values
Precision degradation	Variance of the added noise in $\frac{m^2}{s^4}$	0, 0.05, 0.1, 0.15, 0.2, 0.25, 0.3, 0.35, 0.4, 0.45, 0.5, 0.55, 0.6, 0.65, 0.75, 0.8, 0.9, 0.95, 1
Gain defect	Gain factor Δ	0.5, 0.6, 0.65, 0.7, 0.725, 0.5, 0.75, 0.8, 0.825, 0.85, 0.875, 0.9, 0.925, 0.95, 1
Bias defect	Added acceleration in $\frac{m}{s^2}$	0, 0.1, 0.2, 0.3, 0.4, 0.5, 0.6, 0.7, 0.8, 0.9, 1, 1.1, 1.2, 1.3, 1.4, 1.5

4.2. Simulation Settings

For the following simulations, the 5 × 5 platform array, shown in Figure 2a, is used. Sensors are placed according to sensor settings B and F shown in Figure 5 using 3 and 4 z acceleration sensors per platform. The effect of different quantities and magnitude of sensor defects on the rope fault detection performance by the EKF is examined. Two different rope faults are reviewed: A fault in rope number 1, which is easy to detected and a rope fault in rope number 8, which is the most difficult to be detected [28]. Rope number 8 goes through platforms 3, 8, 13, 18 and 23 and rope number 1 through platforms 1, 6, 11, 16 and 21 shown in Figure 2a.

For rope fault detection, the EKF was launched 400 s after the simulation start of the MBD model. The stiffness of the faulty rope was set to 80% of its non-faulty rope after 410 s. Sensor defects are set simultaneously with the EKF start. Simulations are done for a wind speed of 21 m/s measured 19.5 m over sea level, the parameters for the simulated model are referred to the work of [28]. The EKF estimates the rope stiffness of the 30 platform connecting ropes. It is assumed that a rope fault is correctly detected in the simulated model of the platform arrangement if the rope stiffness of the faulty rope estimated by the EKF falls below 95% of the non-faulty rope stiffness within 300 s after the occurrence of the rope fault.

The procedure to represent the influence of the number and parameters of defect sensors on the reliability of rope fault detection is shown in a reference configuration in Figure 8a for 3 and 4 z acceleration sensors per platform.

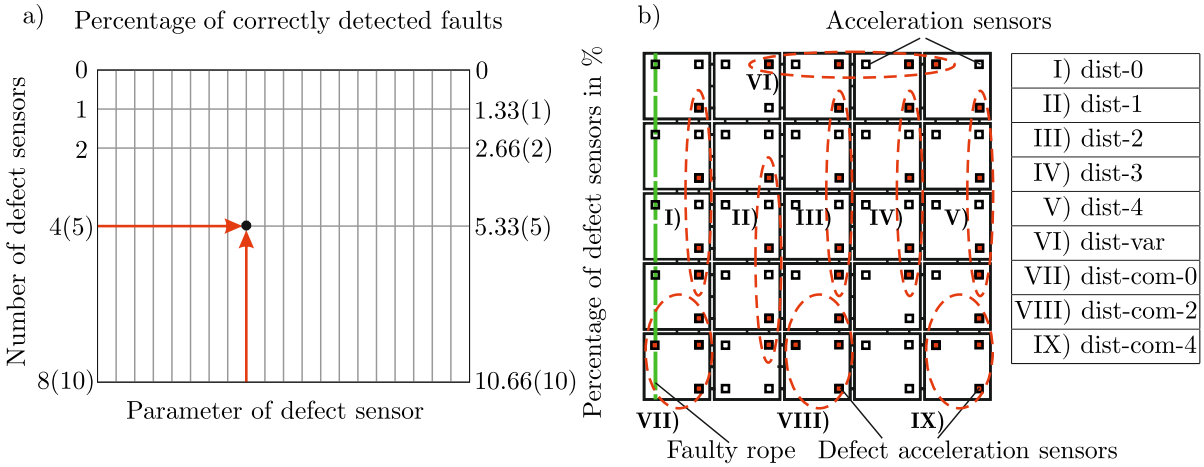

Figure 8. (**a**) Array of the percentage of correctly detected rope faults as a function of number, percentage and parameters of defect sensors for 3 and (4) z acceleration sensors. (**b**) Examples of different distances between 4 defect sensors, a rope fault in rope number 1 and 3 z acceleration sensors per platform.

The horizontal axis in Figure 8a gives the parameter of the defect sensors, the vertical axis the number and percentage of defect sensors per platform arrangement. For every

parameter of the defect sensors, as listed in Table 2, simulations are computed with faultless sensors and 4 different numbers of defect sensors, as shown in Table 3 for sensor setting B and F with 3 and 4 acceleration sensors per platform. The number of simulations in Table 3 is adapted, to get the same number of simulations for every number of defect sensors. Simulations with two different sensor settings are calculated to show to what extent the usage of an additional sensor per platform is beneficial.

Table 3. Number of defect sensors per platform arrangement and number of simulations calculated for the respective number of defect sensors executed for rope fault detection in rope number 1. The indices * at the distances between the platforms with the defect sensors and the platforms with the rope fault, dist-0 to dist-4, indicates that the defect sensors also occur at adjacent platforms to the given distance at the simulations with 8 and 10 defect sensors.

	Number of Defect Sensors			
Sensors setting B	1	2	4	8
Sensors setting F	1	2	5	10
	Number of simulations			
dist-0 *	2	2	1	1
dist-1 *	2	2	1	1
dist-2 *	2	2	1	1
dist-3 *	2	2	1	1
dist-4 *	2	2	1	1
dist-var	-	-	2	2
dist-com-0	-	-	1	1
dist-com-2	-	-	1	1
dist-com-4	-	-	1	1

For better comparability of the percentage sensor defects, the simulations with 5 and 10 defect sensors are done for the sensor setting F with 4 acceleration measurements per platform, and simulations done with 4 and 8 defect sensors for sensor setting B with 3 acceleration measurements per platform.

4.3. Influence of the Distance between the Platforms with the Defect Sensors and the Platforms with the Rope Fault

Furthermore, the influence of the distance between the platforms with the defect sensors and the platforms with the rope fault is considered. For every different number of defect sensors, simulations with varying distances between the defect sensors and the rope fault are executed. Examples for 4 defect sensors of the 5 × 5 platform array with 3 z acceleration sensor per platform, are shown in Figure 8b. The distance between the platforms with the defect sensors and the platforms with the rope fault is indicated by dist-0 up to dist-4. For dist-0, the sensor defects occurs on the same platform; for dist-1 on the adjacent platform and for dist-2 up to dist-4, there are one to three platforms between the defect sensor and the rope fault. Sensor defects occurring arbitrarily distributed over all platforms are indicated by dist-var, dist-com indicates if more than one sensor defect appears on the same platform. For every number of defect sensors and sensor defect parameter, simulations with different distances listed in Table 3 are calculated. The number of simulations calculated for the respective number of defect sensors per platform arrangement and respective different distances between the defect sensors and the rope fault in rope number 1 is listed in Table 3. The indices * indicates that the defect sensors at simulations using 8 and 10 defect sensors also occur at adjacent platforms to the given distance, which is required for the analysis of one defect sensor per platform. The respective platforms with the defect sensors are listened in Supplementary Material Table S1. For dist-com, the subscript indices in Supplementary Material Table S1 indicates the number of defect sensors on the respective platform. All simulations are done 5 times for the same wave spectrum but a different time-depending wave height curve. These results in 50

fault detection simulations for every number and parameter of the defect sensors and rope fault detection in rope number 1. Based on these simulations, the percentage of correctly detected rope faults is calculated. Figure 8a gives an example of the calculation with 4 respectively 5 defect sensors for one selected sensor defect parameter calculated for the different distances between the defect sensors and the rope fault listed in Table 3.

5. Results of Sensor Defects on the Reliability of Rope Fault Detection by the EKF

The first part of this section presents the influence of sensor precision degradation, sensor gain and sensor bias defects on the rope fault detection reliability. Afterward the influence where defect sensors occur in the platform arrangement and the distance between defect sensors and rope faults on the rope fault detection performance is examined. In the final step, the impact of multiple defect sensors, occurring on the same platform, on the rope fault detection reliability is given.

5.1. Influence of Sensor Precision Degradation, Sensor Gain and Sensor Bias Defects on Rope Fault Detection

Figures 9, 11 and 13a,b show the percentage of correctly detected rope faults, using 3 and 4 z acceleration sensors per platform, as a function of number, percentage and parameters of defect sensors. The dark areas in Figures 9, 11 and 13a,b show simulation settings for defect sensors where the reliability of fault detection is the lowest. When comparing Figures 9, 11 and 13a with Figures 9, 11 and 13b, it has to be considered, that one and two defect sensor equates a bit higher percentage using 3 acceleration sensors per platform instead of 4. Figures 10, 12 and 14 show the advantage using 4 instead of 3 z acceleration sensors per platform. The dark areas show simulation settings for defect sensors where the advantage of using 4 instead of 3 z acceleration sensors is greatest. The different percentage of defect sensors, using 3 acceleration sensors, is respected by interpolation.

Figure 9 shows the influence of sensor precision degradation on the reliability of rope fault detection in rope number 1 by the EKF.

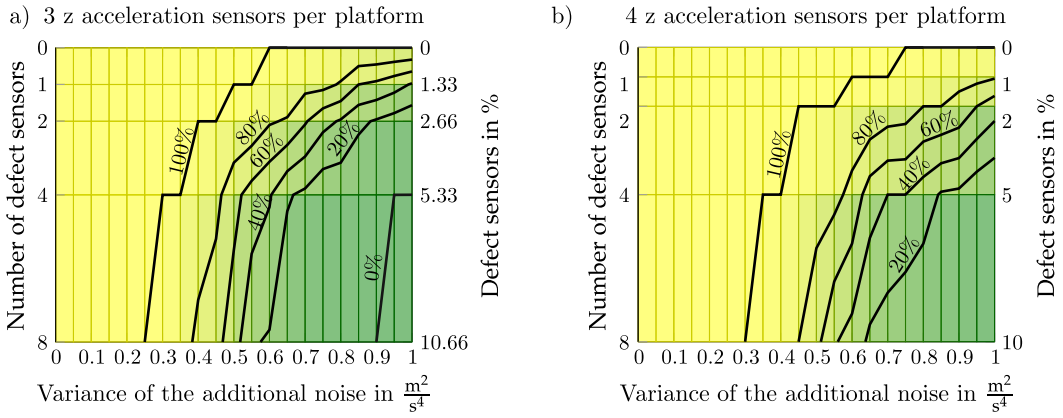

Figure 9. Impact of sensor precision degradation on the percentage of correct detected rope faults by the Extended Kalman Filter (EKF) rope fault estimation for a rope fault in rope number 1. (**a**) 3 z acceleration sensors and (**b**) 4 z acceleration sensors per platform are used.

Figure 9a represents fault detection using 3 z accelerators per platform. Sensor precision degradation simulated by an additional noise with a variance under 0.25 m^2/s^4 has no influence on rope fault detection with up to 8 defect sensors per platform; for two defect sensors, all ropes are detected correctly up to an additional noise with a variance of 0.55 m^2/s^4. Fewer defect sensors result in higher tolerable additional sensor noise. For a defect sensor with additional noise over 0.8 m^2/s^4, already one defect sensor results in unreliable rope fault detection, where at least 20% of the faulty ropes are not detected correctly. The usage

of 4 acceleration sensors per platform leads to a significant improvement of fault detection as shown in the comparison of Figure 9a,b. Using 4 acceleration sensors per platform, one of which is defective in the platform arrangement, leads to at least 80% correctly detected rope faults in rope number 1 as long as the variance of the additional noise is lower than 1 m^2/s^4. Figure 10 shows that the benefit of using 4 instead of 3 z acceleration sensors per platform is significant for an additional sensor noise around 0.85 m^2/s^4 and 1 up to 5% of defect sensors and an additional sensor noise around 0.55 m^2/s^4 and 5 up to 10% of defect sensors.

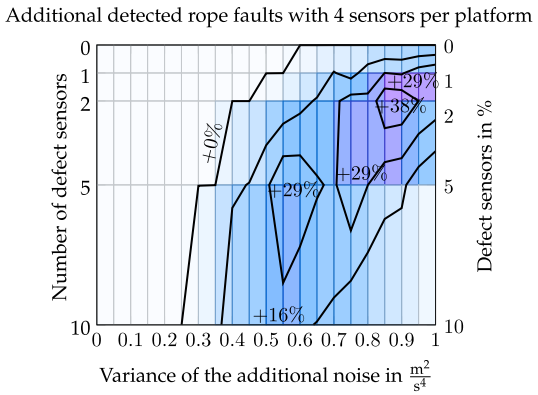

Figure 10. Improvement of fault detection using 4 z acceleration sensors with sensor precision degradation.

Figure 11 represents the influence of sensors with gain defects on the number of correctly detected rope faults in rope number 1.

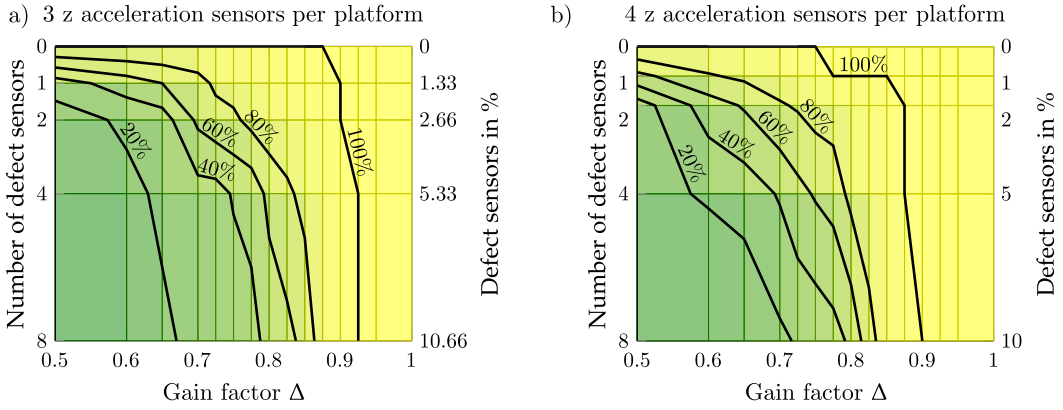

Figure 11. Impact of sensor gain defects on the percentage of correct detected rope faults by the EKF rope fault estimation for a rope fault in rope number 1. (**a**) 3 z acceleration sensors and (**b**) 4 z acceleration sensors per platform are used.

Faults are detected with the highest reliability when the gain factor is not less than 0.92 and 3 acceleration sensors are used per platform, as shown in Figure 11a. Using 4 accelerators per platform, a gain factor higher than 0.90 leads to 100% correctly detected rope faults as shown in Figure 11b. For one sensor gain defect, even a sensor gain loss up to 22.5% results in 100% correctly detected faults, using 4 acceleration sensor per platform, compared to a maximum allowed sensor gain loss of 10% using 3 acceleration sensors per platform. The highest benefit is obtained for 10% of defect sensors and a gain factor around 0.85 m/s^2. Figure 12 shows the advantage of using 4 instead of 3 acceleration sensors per platform.

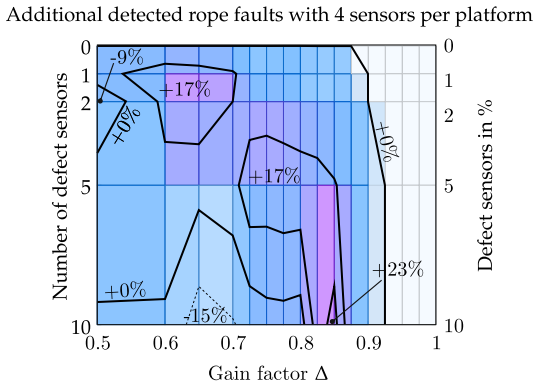

Figure 12. Improvement of fault detection using 4 z acceleration sensors with sensor gain defects.

Figure 13 shows the influence of sensor bias defects on the reliability of rope fault detection in rope number 1 by the EKF.

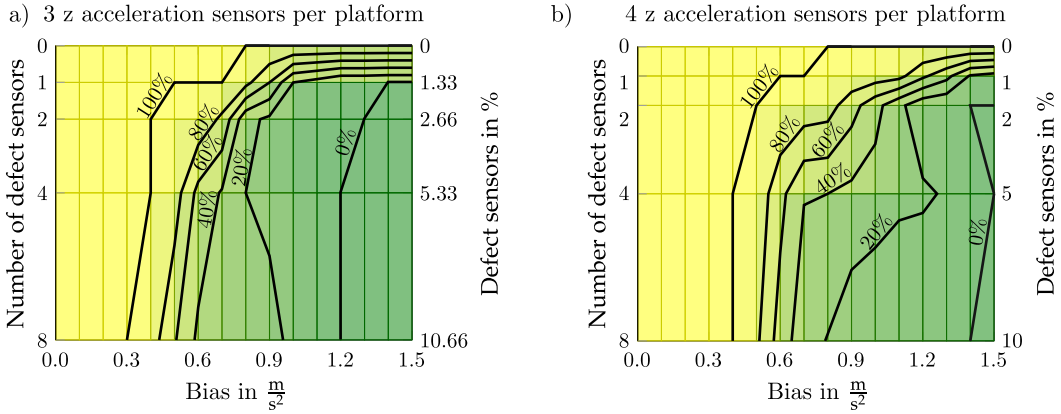

Figure 13. Impact of sensor bias defects on the percentage of correct detected rope faults by the EKF rope fault estimation for a rope fault in rope number 1. (**a**) 3 z acceleration sensors and (**b**) 4 z acceleration sensors per platform are used.

A sensor bias up to 0.3 m/s^2 respectively 0.35 m/s^2 has no influence on the reliability of rope fault detection as shown in Figure 13a,b. The gradient of the line indicating the contour of 20% correctly detected faults in Figure 13a shows that the allowed sensor bias for four defect sensors is lower than for eight defect sensors. A higher number of sensor bias defects with the same bias on adjacent sensors and platforms where all sensors are defect, influences the estimation of the states and rope parameters of the MBD model by the EKF and the overall dynamic of the estimated platform model in a way that can have a positive effect on the rope fault estimation algorithm. Locations of defect sensors where this effect occurs are named dist-com and listed in Supplementary Table S1. A larger sector in the platform arrangement, containing eight instead of four bias sensor defects, has less negative impact on estimating the whole platform array's x and y movement, almost mainly the z states of the platform section with the defect sensors are estimated wrong. This leads to a more reliable estimate of the rope stiffness by the EKF. Figure 13b shows that five defect sensors may allow a higher sensor bias than two defect sensors to detect 20% of the rope faults in rope number 1 correctly. The simulations with five defect sensors also contain simulations with platforms where all sensors are defect leading to a smaller influence on the estimation of the platform x and y movement dynamics of these platforms. This leads to a smaller impact of the defect sensors on the correct rope fault estimation even if there are more defect sensors. Only 20% of correctly detected rope faults are rarely acceptable for practical application. The advantage of using 4 instead of 3 acceleration sensors per

platform is greatest for a sensor bias around 1 m/s^2 and 1% of defect sensors as shown in Figure 14. The maximum increase of additional detected rope faults is 52%.

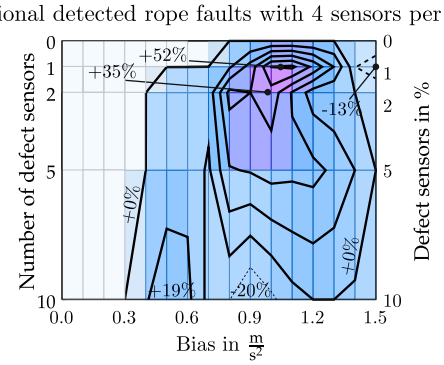

Figure 14. Improvement of fault detection using 4 z acceleration sensors with sensor gain defects.

Figures 12 and 14 show that there are also regions with a negative effect on rope fault detection using 4 instead of 3 acceleration sensors per platform. The region in Figure 12 with a sensor gain factor of 0.5 and two defect sensors and the region in Figure 14 with a sensor bias of 1.5 and one defect sensor results from interpolating the percentage of correct detected rope faults using 3 z acceleration sensors per platform. 10% of defect sensors and a sensor gain factor lower than 0.8 in Figure 12 and a bias around 0.9 in Figure 14 results and in fewer correctly detected rope faults. An additional sensor per platform may lead to fewer correctly detected rope faults when sensor gain or sensor bias defects occur. Defect sensors lead to worse results for state and parameter estimation by the EKF. If there are two platforms side by side where all sensors are defective, named dist-com in Supplementary Table S1 and Table 3, state and parameter estimation of these platforms leads to even worse results using 4 instead of 3 z acceleration sensors per platform. The incorrectly estimated states and parameters of these platforms are compensated to a greater extent by the surrounding platforms without defect sensors when only 3 sensors per platform are attached to and defect. If the correctly detected rope faults due to this phenomenon predominate the correctly detected rope faults in the simulations with only one defect sensor per platform and using 4 instead of 3 acceleration sensors per platform, this leads to the negative regions at 10% of defect sensors per platform arrangement in Figures 12 and 14. This phenomenon mainly occurs at a higher number of defective sensors, as there must be at least 4 defect sensors to obtain all sensors of a platform defect if there are placed 4 acceleration sensors per platform. If there is only one platform where all sensors have a gain or bias defect, the disadvantage of this phenomenon is negligible.

The influence of sensor precision degradation, sensor bias and gain defects on the reliability of rope fault detection in rope number 8 is shown in Supplementary Material Figures S1–S3. The number of simulations calculated for the respective number of defect sensors per platform arrangement and respective different distances between the defect sensors and the rope fault in rope number 8 is listed in Supplementary Material Table S2. The number of simulations in Supplementary Material Table S2 differs to approximate the number of simulations executed for every number of defect sensors. These simulations are performed five times for the same wave spectrum but with a different time-depending wave height curve. The locations of defect sensors for a rope fault in rope number 8 are listed in Supplementary Material Table S1.

5.2. The Influence of the Distance between Defect Sensors and Rope Faults on the Rope Fault Detection Reliability

The values of the following bar plots in Figures 15 and 16 reflect the percentage of correctly detected rope faults averaged over all defect sensor parameters listed in Table 2 and different numbers of defect sensors listed in Table 3 used in the section before. Different distances of the rope faults to the sensor defects are indicated with dist-0 to dist-4. A lower

percentage of correctly detected rope faults means less reliable fault detection. Rope fault detection in rope number 1 and 8 is considered. Figure 15 shows the influence of the distance of rope faults and defect sensors on the rope fault estimation process for a rope fault in rope number 1 using sensor setting B and F with 3 and 4 z acceleration sensors.

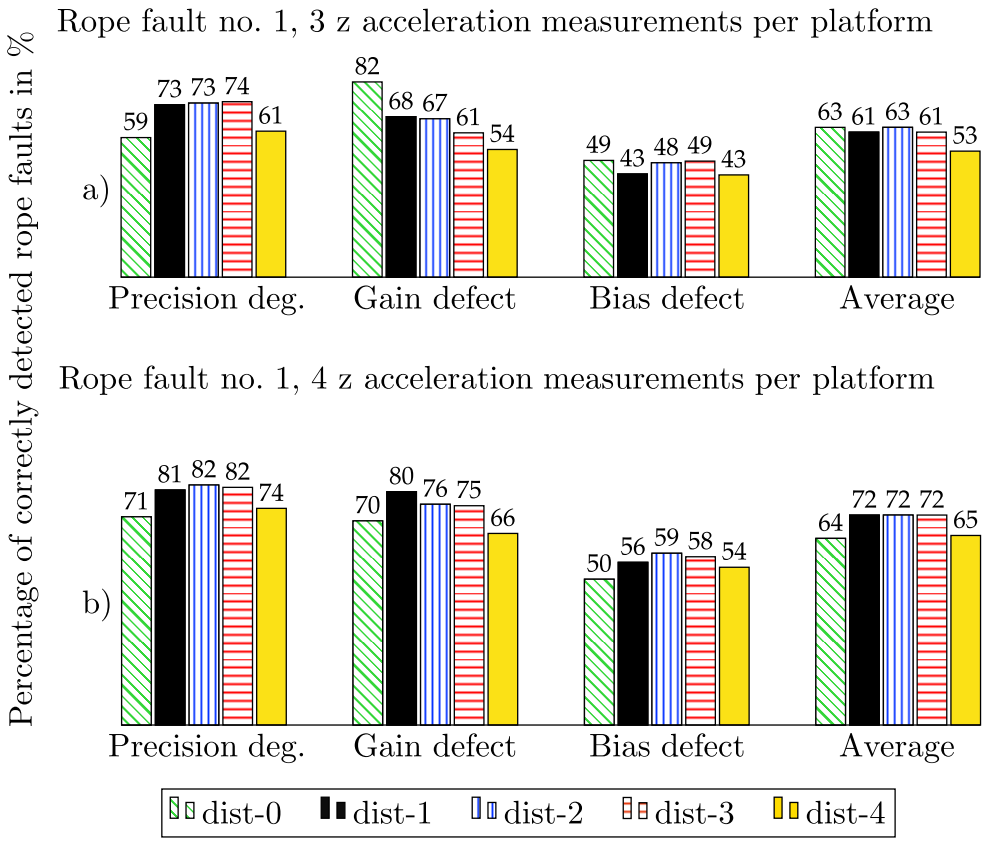

Figure 15. Percentage of correctly detected rope faults depending on the distance between defect sensors and the rope faults for a rope fault in rope number 1. (**a**) 3 z acceleration sensors and (**b**) 4 z acceleration sensors per platform are used.

For better comparability, only single defect sensors per platform are considered. For a rope fault in rope number 1, located on the edge of the platform arrangement, sensor precision degradation leads to the worst results if defect sensors occur at the platforms with the faulty rope or at the platforms with the largest distance to the faulty rope using 3 and 4 acceleration sensors per platform. This is reflected in a lower percentage of correctly detected rope faults when the distance between defect sensors and the rope fault is dist-0 and dist-4. The same phenomenon can be observed for sensor gain and sensor bias defects using 4 acceleration sensors per platform as shown in Figure 15b. The average percentage of correctly detected rope faults indicates the average percentage of correctly detected rope faults resulting from the degradation of sensor precision, sensor gain and sensor bias defects. For a rope fault in rope number 8, located in the middle of the platform arrangement, Figure 16a,b show a decreasing rope fault detection rate with an increasing distance between rope faults and defect sensors for all kinds of defect sensors. It is shown that sensor faults occurring closer to the platforms with the rope fault do not have a negative impact on the reliability of the rope fault detection in most cases.

Considering these results, it can be concluded that the percentage of correctly detected rope faults is hardly influenced by the distance between the defect sensors and the rope faults. However, the location of the defect sensors in the platform arrangement influences rope fault detection, where defect sensors occurring at or near the edge platforms of the platform arrangement leads to the worst results for rope fault detection. Defect sensors

occurring on the edge platforms of the platform arrangement are named dist-0 and dist-4 in Figure 15 for a rope fault in rope number 1 and dist-2 in Figure 16 for a rope fault in rope number 8. This effect is based on the attachment of the ropes to the exterior platforms, shown in Figures 2c and 3, whereby changing rope stiffness more influences the dynamic of these platforms. Therefore, the EKF gets more information for state and parameter estimation from the exterior platforms. Incorrect input information to the EKF, generated by anomalous sensor measurement values due to defect sensors of these exterior platforms, leads to worse rope fault detection results than defective sensors occurring further inside the platform array.

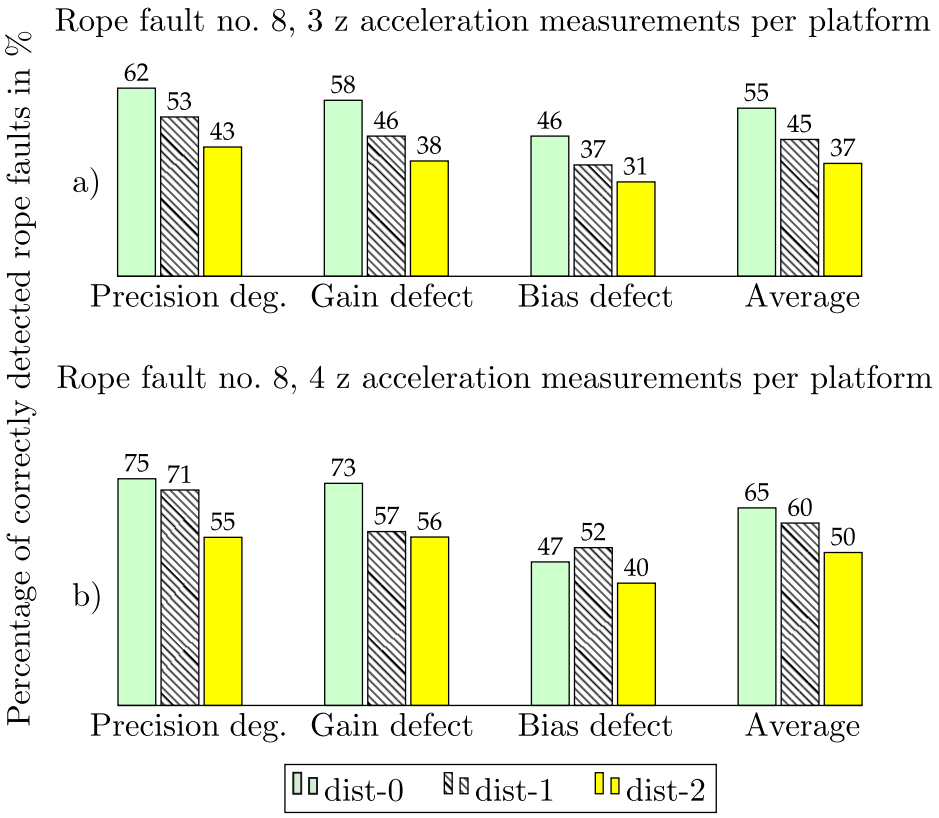

Figure 16. Percentage of correctly detected rope faults depending on the distance between defect sensors and the rope faults for a rope fault in rope number 8. (**a**) 3 z acceleration sensors and (**b**) 4 z acceleration sensors per platform are used.

5.3. The Influence of the amount of Defect Sensors Per Platform on the Rope Fault Detection Reliability

The influence of the number of defect sensors per platform is reviewed for 3 and 4 z acceleration sensors per platform and rope fault detection in rope number 1 and 8. Rope fault detection of single defect sensors per platform is compared to multiple defect sensors per platform, including the influence of the distance of the defect sensors to the rope fault. For rope fault detection in rope number 1, the distances of the defect sensors to the rope fault are named dist-0, dist-2 and dist-4, for rope fault detection in rope number 8 dist-0, dist-1 and dist-2. The placements of the defect sensors on the platform array are listed in Supplementary Material Table S1. For comparability, the total amount of defect sensors per platform arrangement and the distance between defect sensors and the rope fault is kept constant. The percentage of correct rope fault detection shown if Figures 17 and 18 is averaged over all simulations with different sensor defect parameters shown in Table 2.

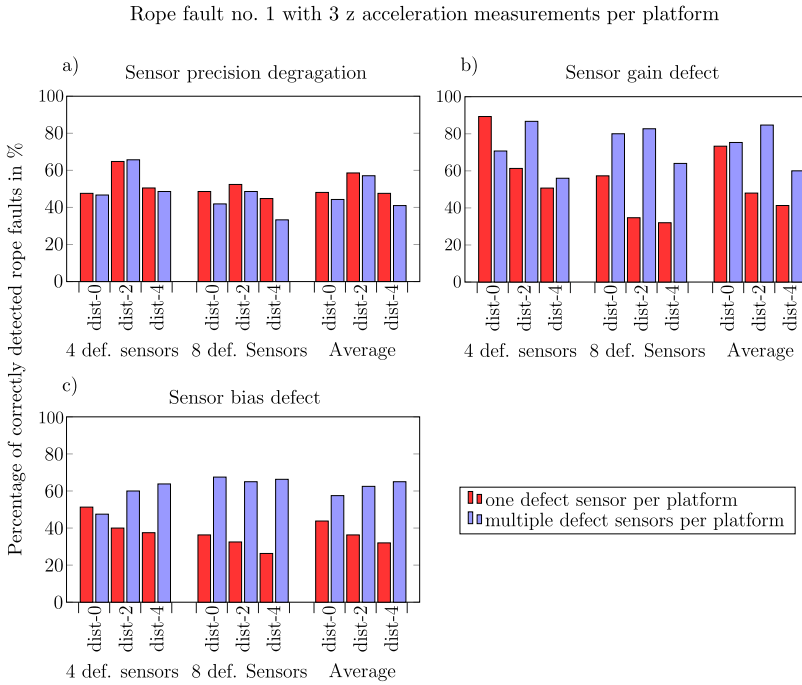

Figure 17. Comparison of single and multiple sensor defects per platform on the reliability of rope fault detection for a rope fault in rope number 1 with 3 z acceleration sensors per platform. Results for three different distances between defect sensors and the rope fault are shown: (**a**) For sensor precision degradation, (**b**) for sensor gain defects and (**c**) for sensor bias defects.

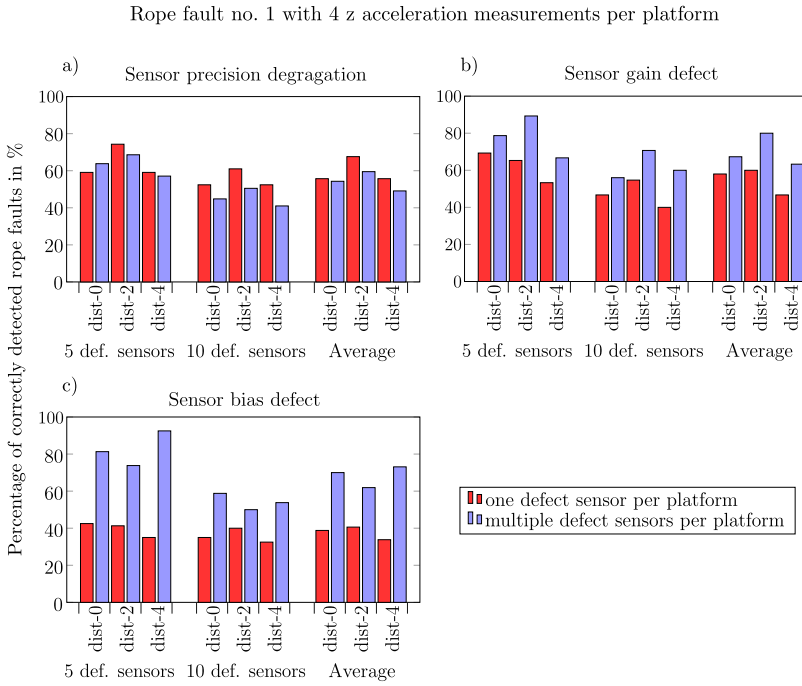

Figure 18. Comparison of single and multiple sensor defects per platform on the reliability of rope fault detection for a rope fault in rope number 1 with 4 z acceleration sensors per platform. Results for three different distances between defect sensors and the rope fault are shown: (**a**) For sensor precision degradation, (**b**) for sensor gain defects and (**c**) for sensor bias defects.

Figures 17a and 18a shows that for sensor precision degradation more defect sensors per platform lead to a negligible difference of correctly detected rope faults in rope number 1. More defect sensors per platform lead mostly to significantly better results for rope fault detection, when sensor gain and sensor bias defects occur as shown in Figure 17b,c for 3 and in Figure 18b,c for 4 z acceleration sensors per platform. When the sensor bias defects of all sensors of a platform are similar, mainly the z state of this platform is estimated wrong by the EKF. This results in deviating estimation of the platform rotation of this platform caused by the ropes and fenders connecting the platform with the adjacent platforms. Although the deviation of the movement estimation in x and y direction of the whole platform arrangement, from the non-faulty sensor platform arrangement, is significantly smaller compared with defect sensors distributed on a higher number of platforms. These effects advantageously influence the estimation of the states and parameters of the platform arrangement for multiple sensor bias defects per platform which leads to a higher percentage of correctly detected rope faults. In the simulations, sensor gain defects are set by multiplying the non-faulty acceleration amplitude by a gain factor. For varying acceleration amplitudes, sensor gain defects result in different sensor amplitude defects. Different sensor amplitude defects occurring at the same platform leads to irregularly distributed defect sensors resulting in a reduced benefit of multiple defect sensors per platform with sensor gain defects compared to sensor bias defects. The comparison of Figures 17b,c and 18b,c shows this difference.

The impact of multiple sensor defects per platform on the reliability of rope fault detection for a rope fault in rope number 8 is shown in Supplementary Material Figures S4 and S5.

6. Conclusions

In the presented work, the Extended Kalman Filter (EKF) technique is used to detect faults in connecting elements of floating modular offshore platforms. Simulations confirm that there is a significant influence of sensor data variation caused by the occurrence of defect sensors, different sensor placements and number of sensors on the rope fault detection reliability. A strategy for optimal placement of the acceleration sensors, which are attached to the platforms, to reduce the number of sensors while maintaining sufficient fault detection reliability is shown. The results are confirmed by the simulation of several test cases with different sensor quantities and sensor placements. Three accelerometers measuring the acceleration in the vertical direction of the platforms are usually sufficient for rope fault detection. The rope fault detection time can be shortened mainly by additional acceleration measurements in vertical direction. Based on the optimal sensor settings, the influence of the numbers, place of occurrence and intensity of sensor defects on the fault detection reliability is reviewed. Results show that the advantages of using an additional sensor per platform for fault detection are predominant, but there are also cases where fault detection reliability is reduced. Furthermore, it is shown that sensor defects occurring on the exterior platforms of the platform arrangement reduce the reliability of rope fault detection more than sensor defects appearing further inside the platform arrangement. It is shown that the influence of the distance between defect sensors and faults in the connecting elements is negligible. Finally, the number of defect sensors per platform are varied, simulations show more reliable fault detection in the connecting elements when sensor defects occur more closely.

Supplementary Materials: The following supporting information can be downloaded at: https://www.mdpi.com/article/10.3390/applmech3030045/s1, Figure S1: Impact of sensor precision degradation on the percentage of correct detected rope faults by the EKF rope fault estimation for a rope fault in rope number 8.; Figure S2: Impact of sensor gain defects on the percentage of correct detected rope faults by the EKF rope fault estimation for a rope fault in rope number 8.; Figure S3: Impact of sensor bias defects on the percentage of correct detected rope faults by the EKF rope fault estimation for a rope fault in rope number 8.; Figure S4: Comparison of single and multiple sensor defects per platform on the reliability of rope fault detection for a rope fault in rope number 8 with 3 z acceleration sensors per platform.; Figure S5: Comparison of single and multiple sensor defects

per platform on the reliability of rope fault detection for a rope fault in rope number 8 with 4 z acceleration sensors per platform.; Table S1: Locations of defect sensors for rope fault in rope number 8 and 1.; Table S2: Number of simulations calculated for the respective number of defect sensors per platform arrangement executed for rope fault detection in rope number 8.

Author Contributions: Conceptualization, A.T.; methodology, A.T.; software, A.T.; validation, K.E. and J.L.; formal analysis, A.T.; investigation, A.T.; writing—original draft preparation, A.T.; writing—review and editing, K.E. and J.L.; visualization, A.T.; project administration, A.T.; funding acquisition, K.E. All authors have read and agreed to the published version of the manuscript.

Funding: Open Access Funding by the Graz University of Technology.

Institutional Review Board Statement: Not applicable.

Informed Consent Statement: Not applicable.

Data Availability Statement: The data presented in this study are available on request from the corresponding author. The data are not publicly available due to an ongoing research project.

Conflicts of Interest: The authors declare no conflict of interest.

Abbreviations

The following abbreviations are used in this manuscript:

KF	Kalman Filter
EKF	Extended Kalman Filter
MBD	Multi body dynamics

References

1. Li, D.; Wang, Y.; Wang, J.; Wang, C.; Duan, Y. Recent advances in sensor fault diagnosis: A review. *Sens. Actuators Phys.* **2020**, *309*, 111990. [CrossRef]
2. Prabowo, A.R.; Tuswan, T.; Ridwan, R. Advanced Development of Sensors' Roles in Maritime-Based Industry and Research: From Field Monitoring to High-Risk Phenomenon Measurement. *Appl. Sci.* **2021**, *11*, 3954. [CrossRef]
3. Von Bock und Polach, R.U.; Ehlers, S. Heave and pitch motions of a ship in model ice: An experimental study on ship resistance and ice breaking pattern. *Cold Reg. Sci. Technol.* **2011**, *68*, 49–59. [CrossRef]
4. Jang, J.; Choi, S.H.; Ahn, S.M.; Kim, B.; Seo, J.S. Experimental investigation of frictional resistance reduction with air layer on the hull bottom of a ship. *Int. J. Nav. Archit. Ocean. Eng.* **2014**, *6*, 363–379. [CrossRef]
5. Drewing, S.; Witkowski, K. Spectral Analysis of Torsional Vibrations Measured by Optical Sensors, as a Method for Diagnosing Injector Nozzle Coking in Marine Diesel Engines. *Sensors* **2021**, *21*, 775. [CrossRef] [PubMed]
6. Penttilä, P.; Ruponen, P. Use of Level Sensors in Breach Estimation for a Damaged Ship. In Proceedings of the 5th International Conference on Collision and Grounding of Ships, Espoo, Finland, 14–16 June 2010; Volume 505, p. 2.
7. Tagesson, T.; Mastepanov, M.; Mölder, M.; Tamstorf, M.P.; Eklundh, L.; Smith, B.; Sigsgaard, C.; Lund, M.; Ekberg, A.; Falk, J.M.; et al. Modelling of growing season methane fluxes in a high-Arctic wet tundra ecosystem 1997–2010 using in situ and high-resolution satellite data. *Tellus Chem. Phys. Meteorol.* **2013**, *65*, 19722. [CrossRef]
8. Goodrich, J.; Oechel, W.; Gioli, B.; Moreaux, V.; Murphy, P.; Burba, G.; Zona, D. Impact of different eddy covariance sensors, site set-up, and maintenance on the annual balance of CO2 and CH4 in the harsh Arctic environment. *Agric. For. Meteorol.* **2016**, *228–229*, 239–251. [CrossRef]
9. Wang, P.; Tian, X.; Peng, T.; Luo, Y. A review of the state-of-the-art developments in the field monitoring of offshore structures. *Ocean. Eng.* **2018**, *147*, 148–164. [CrossRef]
10. Kim, B.; Min, C.; Kim, H.; Cho, S.; Oh, J.; Ha, S.H.; Yi, J.h. Structural Health Monitoring with Sensor Data and Cosine Similarity for Multi-Damages. *Sensors* **2019**, *19*, 3047. [CrossRef]
11. Wu, L.; Maheshwari, M.; Yang, Y.; Xiao, W. Selection and Characterization of Packaged FBG Sensors for Offshore Applications. *Sensors* **2018**, *18*, 3963. [CrossRef]
12. Nichols, J. Structural health monitoring of offshore structures using ambient excitation. *Appl. Ocean. Res.* **2003**, *25*, 101–114. [CrossRef]
13. Beko, M.; Ivosevic, S.; Dlabac, T. Application of Sensors in the Corrosion Monitoring of the Ship's Structural Parts. In Proceedings of the 2021 25th International Conference on Information Technology (IT), Zabljak, Montenegro, 16–20 February 2021; pp. 1–4. [CrossRef]
14. Inaudi, D.; Glisic, B.; Gasparoni, F.; Cenedese, S.; Zecchin, M. Strain sensors for deepwater applications. In Proceedings of the 3rd International Conference on Structural Health Monitoring of Intelligent Infrastructure, Vancouver, BC, Canada, 13–16 November 2007.

15. Ge, M.; Kannala, J.; Li, S.; Maheshwari, H.; Campbell, M. A New Riser Fatigue Monitoring Methodology Based on Measured Accelerations. In Proceedings of the ASME 2014 33rd International Conference on Ocean, Offshore and Arctic Engineering OMAE2014, San Francisco, CA, USA, 8–13 June 2014; p. V06AT04A063. [CrossRef]
16. Liu, Y.; Fontanella, A.; Wu, P.; Ferrari, R.; Wingerden, J.W. Fault Detection of the Mooring system in Floating Offshore Wind Turbines based on the Wave-excited Linear Model. *J. Phys. Conf. Ser.* **2020**, *1618*, 022049. [CrossRef]
17. Hassani, V.; Pascoal, A.; Sørensen, A. Detection of mooring line failures using Dynamic Hypothesis Testing. *Ocean. Eng.* **2018**, *159*, 496–503. [CrossRef]
18. Auger, F.; Hilairet, M.; Guerrero, J.M.; Monmasson, E.; Orlowska-Kowalska, T.; Katsura, S. Industrial Applications of the Kalman Filter: A Review. *IEEE Trans. Ind. Electron.* **2013**, *60*, 5458–5471. [CrossRef]
19. Moreno, V.M.; Pigazo, A. *Kalman Filter*; IntechOpen: Rijeka, Croatia, 2009. [CrossRef]
20. Dan, S. *Optimal State Estimation: Kalman, H Infinity, and Nonlinear Approaches*; Wiley-Interscience: Hoboken, NJ, USA, 2006.
21. Imai, H.; Yun, C.B.; Maruyama, O.; Shinozuka, M. Fundamentals of system identification in structural dynamics. *Probabilistic Eng. Mech.* **1989**, *4*, 162–173. [CrossRef]
22. Brown, S.D. The Kalman filter in analytical chemistry. *Anal. Chim. Acta* **1986**, *181*, 1–26. [CrossRef]
23. Saho, K. Kalman Filter for Moving Object Tracking: Performance Analysis and Filter Design. In *Kalman Filters*; de Oliveira Serra, G.L., Ed.; IntechOpen: Rijeka, Croatia, 2018; Chapter 12. [CrossRef]
24. Van De Wal, M.; De Jager, B. A review of methods for input/output selection. *Automatica* **2001**, *37*, 487–510. [CrossRef]
25. Flikkema, M.; Waals, O. Space@Sea the Floating Solution. *Front. Mar. Sci.* **2019**, *6*, 553. [CrossRef]
26. Schultz-Zehden, A.; Lukic, I.; Onwona, J.; Altvater, S.; Bamlett, R.; Barbati, A.; Barbanti, M.; Buck, B.H.; Calado, H.; Varona, M.C.; et al. Ocean Multi-Use Action Plan. In *Proceedings of the MUSES (Multi-Use in European Seas)*; Multi-Use in European Seas: Edingburgh, Scotland, 2018.
27. Souravlias, D.; Dafnomilis, I.; Ley, J.; Assbrock, G.; Duinkerken, M.B.; Negenborn, R.R.; Schott, D.L. Design Framework for a Modular Floating Container Terminal. *Front. Mar. Sci.* **2020**, *7*, 545637. [CrossRef]
28. Tockner, A.; Blümel, B.; Ellermann, K. Fault Detection in Modular Offshore Platform Connections Using Extended Kalman Filter. *Front. Built Environ.* **2021**, *7*, 658363. [CrossRef]
29. Kim, Y.; Bai, J.W.; Albano, L. Fragility estimates of smart structures with sensor faults. *Smart Mater. Struct.* **2013**, *22*, 5012. [CrossRef]
30. Odgaard, P.; Stoustrup, J.; Nielsen, R.; Damgaard, C. Observer Based Detection of Sensor Faults in Wind Turbines. In Proceedings of the European Wind Energy Conference, Marseille, France, 16–19 March 2009; Volume 7.
31. Ni, K.; Nithya, R.; Chehade, M.; Balzano, L.; Nair, S.; Zahedi, S.; Kohler, E.; Pottie, G.; Hansen, M.; Srivastava, M. Sensor Network Data Fault Types. *ACM Trans. Sen. Netw.* **2009**, *5*, 1–29. [CrossRef]
32. Pierson, W.J., Jr.; Moskowitz, L. A proposed spectral form for fully developed wind seas based on the similarity theory of S. A. Kitaigorodskii. *J. Geophys. Res.* **1964**, *69*, 5181–5190. [CrossRef]
33. Spanos, P.T. ARMA Algorithms for Ocean Wave Modeling. *J. Energy Resour. Technol.* **1983**, *105*, 300–309. [CrossRef]
34. Ma, S.L.; Jiang, S.F.; Li, J. Structural damage detection considering sensor performance degradation and measurement noise effect. *Measurement* **2019**, *131*, 431–442. [CrossRef]
35. Yi, T.H.; Huang, H.B.; Li, H.N. Development of sensor validation methodologies for structural health monitoring: A comprehensive review. *Measurement* **2017**, *109*, 200–214. [CrossRef]
36. Lili, L.; Liu, G.; Zhang, L.; Li, Q. Sensor fault detection with generalized likelihood ratio and correlation coefficient for Bridge SHM. *J. Sound Vib.* **2019**, *442*, 445–458. [CrossRef]